Bioactive Materials 6 (2021) 3437–3448

Contents lists available at ScienceDirect

Bioactive Materials

journal homepage: www.sciencedirect.com/journal/bioactive-materials

Biomimetic Ti–6Al–4V alloy/gelatin methacrylate hybrid scaffold with enhanced osteogenic and angiogenic capabilities for large bone defect restoration

Limin Ma [a,1], Xiaolan Wang [a,c,1], Ye Zhou [b,1], Xiongfa Ji [a], Shi Cheng [a], Dong Bian [a], Lei Fan [c], Lei Zhou [c,***], Chengyun Ning [c,**], Yu Zhang [a,*]

[a] Department of Orthopedics, Guangdong Provincial People's Hospital, Guangdong Academy of Medical Sciences, Guangzhou, Guangdong, 510080, China
[b] Laboratory of Basic Medicine, General Hospital of Southern Theatre Command of the PLA, Guangzhou, 510010, China
[c] School of Materials Science and Engineering, South China University of Technology, Guangzhou, 510641, China

ARTICLE INFO

Keywords:
3D printing porous titanium alloys
Gelatin methacrylate
Angiogenesis
Osteogenesis

ABSTRACT

Titanium-based scaffolds are widely used implant materials for bone defect treatment. However, the unmatched biomechanics and poor bioactivities of conventional titanium-based implants usually lead to insufficient bone integration. To tackle these challenges, it is critical to develop novel titanium-based scaffolds that meet the bioadaptive requirements for load-bearing critical bone defects. Herein, inspired by the microstructure and mechanical properties of natural bone tissue, we developed a Ti–6Al–4V alloy (TC4)/gelatin methacrylate (GelMA) hybrid scaffold with dual bionic features (GMPT) for bone defect repair. GMPT is composed of a hard 3D-printed porous TC4 metal scaffold (PT) backbone, which mimics the microstructure and mechanical properties of natural cancellous bone, and a soft GelMA hydrogel matrix infiltrated into the pores of PT that mimics the microenvironment of the extracellular matrix. Ascribed to the unique dual bionic design, the resultant GMPT demonstrates better osteogenic and angiogenic capabilities than PT, as confirmed by the *in vitro* and rabbit radius bone defect experimental results. Moreover, controlling the concentration of GelMA (10%) in GMPT can further improve the osteogenesis and angiogenesis of GMPT. The fundamental mechanisms were revealed by RNA-Seq analysis, which showed that the concentration of GelMA significantly influenced the expression of osteogenesis- and angiogenesis-related genes via the Pi3K/Akt/mTOR pathway. The results of this work indicate that our dual bionic implant design represents a promising strategy for the restoration of large bone defects.

1. Introduction

Large bone defects are often sequelae of trauma, tumors (osteosarcoma), or congenital diseases [1], and bone autografts are the gold standard for restoration [2,3]. However, the scarcity of bone donors and the time/cost of surgery seriously impede clinical applications [4]. Moreover, allografts harvested from genetically nonidentical species face immune rejection, and high resorption rates can lead to associated complications [5–7]. Therefore, it is still a great challenge to restore large bone defects.

Synthetic biocompatible substitutes based on metals, ceramics, bioactive glasses, and cements are treated as some of the most promising solutions in response to the above challenges [8]. To date, over a million Ti–6Al–4V (TC4) implants have been used for joint replacement and large bone defect restoration every year [9,10] due to the excellent mechanical strength, well-developed CNC processing technologies, biosafety, and corrosion resistance of TC4 [11,12]. However, although TC4 implants are widely used in the clinic, they still have the problems of unsatisfactory life span, bone resorption, and bone nonunion owing to the inert surface of Ti and the mismatched stiffness between Ti-based

Peer review under responsibility of KeAi Communications Co., Ltd.
* Corresponding author.
** Corresponding author.
*** Corresponding author.
E-mail addresses: zhoul@scut.edu.cn (L. Zhou), imcyning@scut.edu.cn (C. Ning), luck_2001@126.com (Y. Zhang).
[1] The authors contributed equally to this work.

https://doi.org/10.1016/j.bioactmat.2021.03.010
Received 18 February 2021; Received in revised form 1 March 2021; Accepted 2 March 2021

implants (~10^2 GPa) and natural bones (~350 MPa for cancellous bone and ~10 GPa for cortical bone) [6,13–15]. To address these problems, diverse strategies have been reported in the modification of Ti-based implants, including element doping, surface plasma treatment, pore structural engineering, active coating, and so on [16–19]. Christine McBeth et al. [20] reported a GelMA scaffold that can be directly printed on and grafted to the titanium implant surface to substantially improve osseointegration of titanium implants. He et al. [21] reported that an optimized scaffold architecture can benefit the ingrowth of bone by utilizing the relatively straight pore for the inner diffusion of chemotactic factors. Nonetheless, although some achievements have been made in facilitating osseointegration, the bone regeneration rate is relatively slow, and the ingrowth depth of new bone in Ti-based implants is shallow [22].

To solve these problems, herein, we develop a GelMA infiltrated Ti–6Al–4V porous scaffold (GMPT) inspired by the heterogeneous microstructure and mechanical properties of natural bone, as shown in Fig. 1. Specifically, the "hard" 3D-printed TC4 metallic scaffold (PT) is designed to mimic the interconnected pore structure and the stiffness of natural bone, which enables the inner growth of new bone and vessels while preventing the issue of autogenous bone resorption. However, even though the apparent stiffness of the PT is close to that of natural bone, the surface of the TC4 material is still too inert to interact with bone-related cells. Therefore, we further design a "soft" GelMA hydrogel matrix that is infilled and chemically anchored in the PT to mimic the bone extracellular matrix (ECM) to help GMPT interact with osteoblast-lineage cells and osteoclasts. Notably, the elastic mechanical properties of GelMA can be easily achieved by rationally controlling the degree of cross-linking density and pore sizes, which allows us to further control the mechanical microenvironment of the ECM for the regulation of new bone formation. With such a unique dual bionic design, our GMPT is expected to be an ideal synthetic substitute with excellent osteogenic and angiogenic capabilities, confirmed by the *in vitro* and rabbit radius bone defect studies, and we discuss the experimental results later.

2. Materials and methods

2.1. Fabrication of 3D-printed porous Ti6Al4V scaffolds

The fabrication process of 3D-printed porous Ti6Al4V scaffolds was identical to our previous work [15]. Specifically, Ti6Al4V powder (Sandvik, Sweden) with a diameter of 15–50 μm was printed into PT scaffolds using a Selective Laser Melting (SLM) 3D printer (Concept Laser M2, Upper Franconia, Germany). The 3D printer is equipped with an Yb-Faser-Laser with a focus beam diameter of 50 μm. The SLM processing occurred under an Ar/N2 atmosphere using a laser (100 W) with a set of scanning conditions (separation, 70 μm; rate, 650 mm/s; layer, 30 μm thick). The PT scaffolds were designed and printed in accordance with an individual bone defect. After SLM processing, the de-powder process was carried out for further use.

2.2. Pretreatment of the PT scaffolds

The surfaces of the PT scaffolds were modified through air plasma treatment and turned into PT-OH. Next, the oxidized PT-OH was immersed in 3-(trimethoxy) propyl methacrylate (TMSPMA) solution (2%, v/v in deionized water) at 37 °C for 2 h. Afterward, the samples were rinsed with alcohol and deionized water, and a nitrogen stream flow was used in the end for drying. The samples subjected to the above process were denoted as PT-TMSPMA.

2.3. Preparation of GelMA

GelMA was synthesized according to the reported protocol [23]. Briefly, 5 g gelatin (Sigma, USA) was dissolved in a water bath at 50 °C. Then, 2 mL methacrylic anhydride (MA) was slowly added into the solution. After complete reaction for 3 h, unreacted MA was removed by centrifugation, and the supernatant solution was dialyzed using a dialysis membrane with a 12-kDa MWCO for one week. Next, GelMA was filtered through a 0.2 μm syringe filter and dehydrated using lyophilization. The processed sample was protected from light and moisture at −20 °C until use. The degree of functionalization (DOF) of GelMA was determined using proton nuclear magnetic resonance (^{1}H NMR) spectroscopy according to a previous report [24]. The peeling force of GMPT was tested using a dynamic thermomechanical analyzer (Q800DE, TA Instruments, America).

2.4. Preparation of the GMPT

First, the photoinitiator Irgacure 2959 (0.5% w/v) was added to the GelMA macromonomer solution in PBS (5%, 10%, 15% w/v). Then, the solution was pipetted between the Ti-TMSPMA and coverslip coated

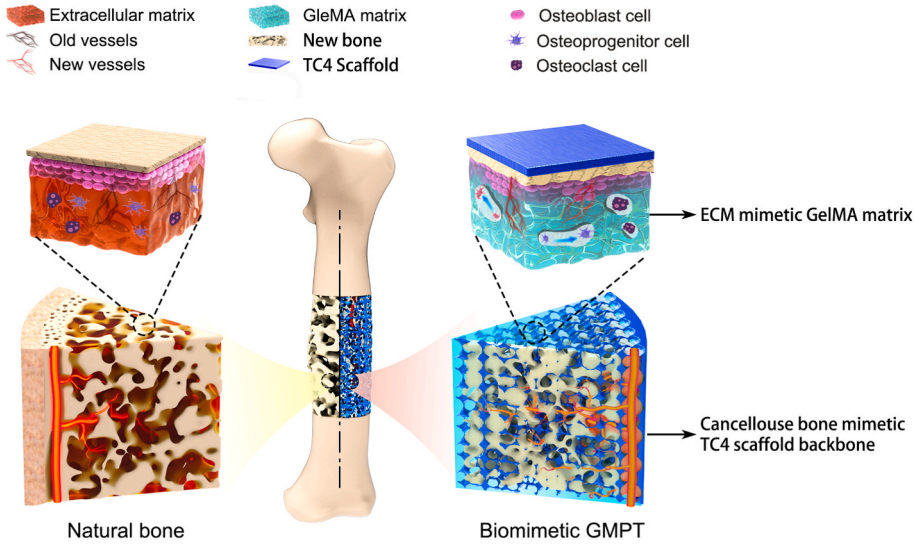

Fig. 1. Schematic illustrations of the biomimetic GMPT with dual-bionic features. The GMPT is composed of a "hard" 3D-printed porous TC4 metal scaffold (PT) backbone which mimics the microstructure and mechanical property of natural cancellous bone, and a "soft" GelMA hydrogel matrix infiltrated in the pores of the PT that mimics the microenvironment of ECM.

with hydrophobic OTS. Next, UV-C light (7.1 mW/cm^2) was used to irradiate the samples from 8 cm away for 80 s. There is space between the PT-TMSPMA and coverslip, which can be adjusted to vary the thickness of the GelMA coatings. Next, the PT scaffolds coated with GelMA were incubated in PBS for 3 h to remove the physically bound GelMA. Last, after lyophilization, the final sample was denoted as PT-GelMA.

2.5. Characterization of the hybrid scaffold structures

The porosity of the PT scaffolds (n = 6) was determined by quantifying their mass and volume. The mechanical properties of the PT scaffolds (5 mm wide, 6 mm high) were evaluated on an MTS 810 material testing system. The structures of the PT scaffolds were imaged using field-emission scanning electron microscopy (FE-SEM, Carl Zeiss AG Merlin, Germany). Their elemental compositions were quantified by energy-dispersive X-ray spectroscopy (EDS, Carl Zeiss AG Merlin, Germany). X-ray photoelectron spectroscopy (XPS, EscaLab Xi+, Germany) was used to measure the surface chemical composition of the specimens. Attenuated total refraction Fourier transform infrared (ATR-FTIR) spectra were recorded with an Avatar 380 FTIR spectrometer (Thermo-Nicolet Nicolet Nexus/Nicolet Continnum, USA) to analyze the chemical composition and structure of the coating. The chemical modification of gelatin was assessed by ^{1}H NMR (Bruker Avance 400 spectrometer, Germany) spectroscopy.

2.6. Binding force experiment

First, two identical GMPT scaffolds were stacked up, and a mechanical testing machine (Q800DE, TA Instruments, USA) pulled the scaffolds apart from opposite directions until the two scaffolds could be separated. The peeling test samples were prepared with a diameter of 13 mm and depth of 2 mm in thickness. The interfacial bonding strength was calculated by a testing machine.

2.7. Static mechanical testing

To evaluate the mechanical properties of GelMA samples, engineered cylindrical samples (ϕ8 mm × 20 mm) were analyzed by compression tests. Mechanical tests were carried out by a universal testing machine (Q800DE, TA Instruments, USA) with a constant deformation rate of 0.05 N/s. The compressive modulus was calculated from the stress–-strain curves in the linear region corresponding to 0–20% strain. Three samples were tested for each hydrogel. The results are presented as the mean ± standard deviation.

2.8. Cell extract and culture

To isolate rabbit bone mesenchymal stem cells (BMSCs), bone marrow from New Zealand white rabbits (4 weeks old) was centrifuged using Percoll (1.073 g/mL, Sigma, USA) according to the manufacturer's instructions. After gradient centrifugation, BMSCs were rinsed using phosphate buffered solution (PBS, Gibco) and incubated in low-glucose Dulbecco's modified Eagle's medium (DMEM-LG, Gibco) with 10% fetal bovine serum (FBS, Gibco). The cells were cultured at 5% CO_2 and saturated humidity. Cells were subcultured using 0.25% trypsin-EDTA solution when they reached 80% confluence. BMSCs at passage three were used in the following experiments.

2.9. Cell viability, proliferation and attachment

To detect the viability and proliferation ability of BMSCs on GMPT and PT scaffolds, 5 × 10^4 cells were seeded on samples for different amounts of time. Then, a cell counting kit-8 (CCK-8) assay was adopted to evaluate cell proliferation after culture for 1, 3, 5, and 7 days followed by the reported protocols. After culturing for 1 day, cell viability was confirmed by live/dead assay. For cell morphology and spreading observation, the cells on the scaffolds were fixed and incubated with FITC phalloidin and DAPI for cytoskeleton and cellular nuclei staining, respectively. Then, the samples were observed under confocal laser scanning microscopy (CLSM, Leica, Japan). To further acquire the detailed BMSC morphology on scaffolds, cells were fixed and dehydrated in ascending concentrations of ethanol (30, 50, 75, 90, 95, and 100 v/v% for 10 min at each gradient) and then observed by SEM.

2.10. Osteogenesis evaluation

To evaluate the osteogenic properties of MSCs cultured on scaffolds, the activity of alkaline phosphatase (ALP) was determined by the ALP test according to the manufacturer's instructions (Thermo Scientific, USA) in osteogenesis-induced medium (Cyagen Biosciences, USA) on days 7 and 14, respectively. A BCA protein assay kit was used to detect the total protein concentration of each cell lysate. Next, the ALP levels were normalized to the total protein content. BMSC matrix mineralization (1 × 10^4 cells/mL) was evaluated by Alizarin red (AR) staining following a published protocol [15]. Quantitative analysis of AR was performed with the addition of 10% cetylpyridinium chloride, followed by measurement of the optical density (OD) at 600 nm using a microplate reader (Thermo Fisher, USA). Both qualitative and quantitative analyses were carried out in this test.

2.11. Angiogenesis evaluation

A tubule-forming assay was used to evaluate the *in vitro* angiogenesis of GMPT and PT scaffolds. The cultured medium of MSCs cultured on the scaffolds was collected at 1 day. Human umbilical vein endothelial cells (HUVECs, ATCC, USA) were incubated at a density of 5 × 10^4 cells per well in a 24-well plate with Matrigel™ (BD Biosciences, USA) coating, in which the culture medium consisted of collected medium:fresh medium at a ratio of 1:1. After culturing for 24 h, the tubules formed in each group were stained with calcein-AM and imaged using a fluorescence microscope. ImageJ software was applied for quantitative analysis.

2.12. Quantitative real-time PCR (RT-PCR) analysis

Using the primers listed in Tables S1 and S2 and glyceraldehyde-3-phosphate dehydrogenase (GAPDH) as a reference, RT-PCR was performed to evaluate the mRNA level of the genes related to osteogenesis and angiogenesis. After the BMSCs were cocultured with the GMPT and PT scaffolds for 7 and 14 days, the expression of osteogenesis-related genes including ALP, osteocalcin (OCN), osteopontin (OPN), type I collagen (Col-I), and runt-related transcription factor 2 (Runx2) was confirmed by RT-PCR. The angiogenesis-related genes expressed by HUVECs included hypoxia-inducible factor-1α (HIF-1α), kinase insert domain-containing receptor (KDR), vascular endothelial growth factor (VEGF) and Drosophila mothers against decapentaplegic 1 (Smad 1). RT-PCR was performed after the HUVECs were cultured on GMPT and PT scaffolds for 3 and 10 days. Briefly, total RNA was extracted using RNA extraction reagent (OMEGA, China) according to the manufacturer's instructions. After determining the concentration and purity of the extracted RNA spectrophotometrically using a Nanodrop 2000 (Thermo Fisher, USA), 1 mg total RNA was acquired for reverse transcription using the 1st Strand cDNA Synthesis SuperMix Kit (Yeasen, China). Synthesized cDNA was then mixed with SYBR Green Mastermix and primers to quantify the expression of osteogenesis- and angiogenesis-related genes. The CT value of each gene was recorded and calculated using the $2^{-\Delta\Delta}$CT method.

2.13. RNA sequencing (RNA-seq) and bioinformatic analyses

The MSC cell line C3H10T1/2 (ATCC) was used to unravel the underlying mechanism [25]. Total RNA was isolated from cells cultured on

10% GMPT and PT scaffolds using TRIzol Reagent (Thermo Fisher Scientific, USA) followed by the RNeasy Plus Mini Kit (Qiagen, USA) according to the manufacturer's instructions. The quantity and integrity of RNA were assessed using FastQC and RSeQC software [26]. Then, the cleaved RNA fragments were reverse-transcribed to create the final cDNA library in accordance with the protocol for the mRNA-Seq sample preparation kit (Illumina). We performed paired-end sequencing on an Illumina HiSeq 2500 at LC Bio (Zhejiang, China) following the vendor's recommended protocol. Paired-end clean reads were mapped to the *Mus musculus* genome. Fragments per kilobase of exon model per million mapped reads (FPKM) were used to measure mRNA abundance using Hisat software. The differentially expressed mRNAs were selected with log2 (fold change) $>$ 1 or log2 (fold change) $<$-1 and with statistical significance (p-value $<$ 0.05) by the edgeR package. Gene ontology (GO) (http://www.geneontology.org) enables functional interpretation of gene and gene product attributes. Bioinformatic analysis was performed using the OmicStudio tools at https://www.omicstudio.cn/tool.

2.14. Intracellular flow cytometry (FCM)

Single-cell suspensions of MSCs cultured on PT, 5% GMPT, 10% GMPT and 15% GMPT for 24 h were prepared using Accutase™ (Invitrogen, USA). After treatment, the cells were fixed and permeabilized using Cytofix fixation buffer and Phosflow Perm buffer III (BD, USA), respectively. FITC-labeled phospho-PI3K p85/p55 antibody, APC-labeled phospho-AKT1 (Ser473) antibody and PE-labeled phospho-mTOR (Ser2448) antibody (eBioscience, China) were used to stain phosphorylated signaling molecules. The stained cells were examined via a Beckman cytoFLEX FCM system, and the obtained results were analyzed using FlowJo™ software.

2.15. Animals and surgical procedures

The experiment was carried out in accordance with the Declaration of Helsinki and was approved by the Ethical Committee of Guangdong Province People's Hospital. New Zealand rabbits were randomly divided into four groups (each group with 6 rabbits): the PT and 5%, 10%, and 15% GMPT groups (weight approximately 2.5 kg, n = 24). Intravenous anesthesia was applied using a solution (3%) of phenobarbital sodium at a dose of 0.5 mL/kg. Muscle relaxation was applied by xylazine hydrochloride at a dose of 0.1 mL/kg. To expose the middle of the lateral radius, a 2.0 cm incision was performed, and osteotomy was then implemented to create a 1.5 cm bone defect along the longitudinal axis of the radius. After complete hemostasis, the 3D-printed scaffolds were implanted to fill the bone defect (Fig. 5a–b). Finally, cautious irrigation was taken before suturing the incision. After the surgery, rabbits were cared for in cages with regular diet and water. Postoperative antibiotic penicillin (100,000 U) was injected consecutively for 3 days into each rabbit.

2.16. Direct mechanical testing

A universal testing machine (Q800DE, TA Instruments, USA) was applied to evaluate the integrated strength between the implant and the bone at 12 weeks. The loading device descended at a constant speed of 0.05 N/s until the implant and bone interface were separated. The push-out stress of the specimen is recorded when there is a sudden drop observed in the load-displacement curves. Six specimens were calculated in each group at different time points.

2.17. Microcomputed tomography (Micro-CT) analysis

Four and 12 weeks postsurgery, the rabbits were sacrificed, and the radiuses with scaffolds were immediately scanned with micro-CT (Latheta, Tokyo, Japan) to evaluate new bone formation [15]. The scanning parameters were set at 80 kV and 40 μA, with 48 μm resolution. The area of the implant was selected as the region of interest (ROI). The percentage of bone volume out of the ROI (BV/TV) was calculated using VG Studio MAX software. The threshold for bone was defined in the range of 226–1600, while the threshold for scaffolds was 500–1600. Beam hardening correction was used to decrease metal artifacts in the micro-CT results.

2.18. Histopathological analysis

The rabbit radiuses with implants were fixed in formalin, dehydrated with ethanol, and then embedded in polymethylmethacrylate (PMMA) (six rabbits per group). The embedded specimens were cut, ground, and polished. Van Gieson's and Masson's trichrome staining were used to assess soft-tissue in-growth and bone formation [27]. The stained sections were imaged by a microscope (Zeiss AX10 imager M2, Germany).

2.19. Immunofluorescence staining

Tissue slices were washed with PBS and infiltrated with 0.1% Triton-100. The nonspecific sites were then blocked with 3% bovine serum albumin (BSA) for 1 h and then incubated with mouse anti-CD31 primary antibody (Abcam, USA) at 4 °C overnight. After PBS washing, the slices were stained with goat anti-mouse IgG (Alexa Fluor 647) (Abcam, USA) and incubated at 27 °C for 4 h. Finally, DAPI was added for 10 min to observe the nuclei before observation. These slices were then scanned and captured with a fluorescence microscope (Olympus, Japan).

2.20. Statistics analysis

The results are presented as the mean ± SD (standard deviation). All data were acquired from three to five independent experiments. Statistical differences were determined using ANOVA via GraphPad Prism 6.0 software. Statistical significance was accepted at *p $<$ 0.05, **p $<$ 0.01, and ***p $<$ 0.001.

3. Results and discussion

3.1. Preparation and characterization of the GMPT scaffolds

Solid bonding between GelMA and PT is important for the mechanical stability of the resultant GMPT. To immobilize GelMA hydrogels onto the surface of 3D-printed PT, 3-(trimethoxysilyl) propyl methacrylate) (TMSPMA) was used as a linker. The Ti scaffolds were first modified as Ti–OH and then immersed in TMSPMA solution to produce Ti-TMSPMA, which formed tight bonds between the saline molecules from TMSPMA and –OH groups from the Ti surface. Next, the GelMA hydrogel polymer was grafted onto Ti-TMSPMA surfaces by applying a photocrosslinking reaction. During the photochemistry immobilization process, GelMA and the –CH═CH_2 groups from TMSPMA were covalently bound. The details on the modification and anchoring process are shown in Fig. 2a. For the control group, we attached the GelMA hydrogel into the pores of the PT by physically entering without chemical bonding.

The chemical composition of the hybrid scaffold was further detected by several methods. As shown in Fig. S1, methacrylate groups present at δ 5.6 and δ 5.8 ppm indicated the successful fabrication of GelMA from gelatin. The presence of Si2p signals (Fig. S2) at 103.2 eV demonstrated that the silane molecules from the TMSPMA molecular bridge were successfully anchored onto the Ti surface. In addition, EDS spectra showed that GelMA mainly consisted of C, N and O (Fig. 2b), and the GelMA-PT scaffold included Ti, Al, V, C, O, and N (Fig. 2c). Further analysis of the GelMA hydrogel on the PT surface was tested by FTIR (Fourier transform infrared) spectroscopy (Fig. S3). The results revealed that hydrogels on PT exhibited the typical amide bands of gelatin protein, including N–H stretching at 3310 cm^{-1} for amide A, C–H stretching at 3063 cm^{-1} for amide B, C–O stretching at 1657 cm^{-1} for amide I, N–H

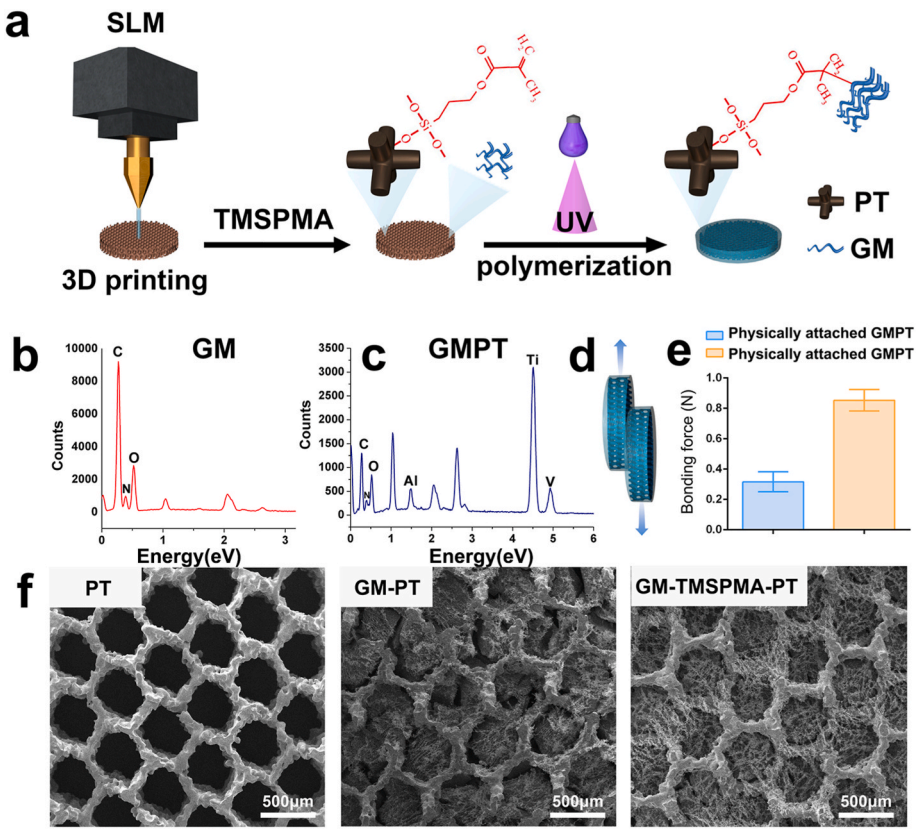

Fig. 2. The fabrication process and characterization of GMPT. (a) Schematic illustration of the fabrication of GMPT. TMSPMA was used as a linker to immobilize GelMA hydrogels onto the surface of 3D-printed PT, thus generating hard-soft hybrid 3D scaffolds. (b, c) The presence of Ti, Al, V, C, O, and N elements in the EDS indicated that GelMA was successfully immobilized on the scaffolds. (d) Schematic illustration of the binding force experiment. (e) The binding force of physically attached GMPT (GM-PT) and chemically anchored GMPT (GM-TMSPMA-PT) (n = 3). (f) SEM images of GelMA and PT scaffolds presented in PT, GM-PT, GM-TMSPMA-PT. Scale bar, 500 μm.

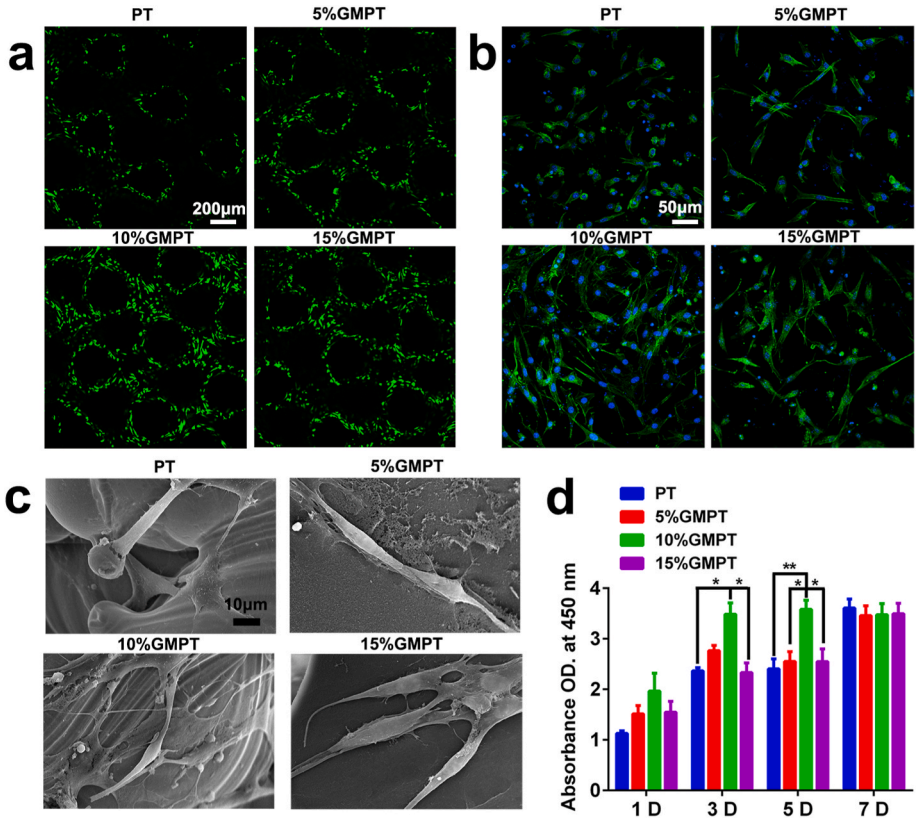

Fig. 3. *In vitro* viability, proliferation and attachment of PT&GMPT hybrid scaffolds (BMSCs as a cell model). (a) Live/dead assay of BSMCs cultured on PT, 5% GMPT, 10% GMPT and 15% GMPT for 1 day. Scale bar, 200 μm. (b) Phalloidin-DAPI staining of HUVECs attached to PT, 5% GMPT, 10% GMPT and 15% GMPT on day 1. Scale bar, 50 μm. (c) SEM of BMSCs attached to PT, 5% GMPT, 10% GMPT and 15% GMPT for 1 day. Scale bar, 20 μm. (d) CCK-8 assay of BMSCs on PT, 5% GMPT, 10% GMPT and 15% GMPT for 1, 3, 5 and 7 days. All scaffolds exhibited excellent cytocompatibility and provided a desirable environment for cell attachment and ingrowth. Asterisks indicate significant differences, * represents $P < 0.05$, ** represents $P < 0.01$.

deformation at 1555 cm^{-1} for amide II, and N–H deformation at 1239 cm^{-1} for amide III, confirming the presence of GelMA.

We then carried out a peeling test to measure the interfacial bonding strength between the hydrogel and PT. A stark difference was observed between the chemically bonded and physically attached PT-GelMA (Fig. 2d). The peeling force of chemically bonded PT-GelMA-PT is approximately three times that of physically attached PT-GelMA-PT (Fig. 2e). The above results indicated that chemically anchoring hydrogels on PT substrates can lead to stronger hydrogel bonding. In addition, as shown in Fig. 2f, distinct differences in SEM (scanning electron microscopy) photographs between the chemically bonded and physically attached hydrogels can be found. The chemically bonded hydrogels were tightly attached to the surface of the scaffold pores. In contrast, obvious gaps can be observed between the physically attached hydrogels and the pores.

We further evaluated the mechanical properties of our GMPT scaffold since it will dramatically influence the supporting performance and the adhesion, proliferation and differentiation of stem cells. In our work, the maximum compressive strength of PT was 47 MPa, which is consistent with the strength of the rabbit radius. The compression modulus of GelMA hydrogels is approximate to the reported suitable stiffness for osteogenesis, which ranges from 7.5 kPa to 25 kPa with increasing GelMA concentration from 5% to 15% (Fig. S4). The compressive strength of the overall GMPT scaffolds was approximately 46 MPa (Fig. S5) despite different GelMA concentrations, which indicated that the surface coating hydrogel basically had no effect on PT stiffness scaffolds.

3.2. Viability, proliferation and adhesion of BMSCs on GMPT scaffolds

The cell toxicity of GMPT and PT scaffolds was tested by the live/dead assay. Toluidine blue staining showed almost no dead cells in any group (Fig. 3a) after 24 h, indicating the high cytocompatibility of GMPT and PT scaffolds. In addition, the number of cells cultivated in GMPT far surpassed that in the PT group, which suggested that the addition of GelMA enhanced cell viability. In particular, GMPT with a GelMA concentration of 10% presented the best cell viability, meaning that the optimal GelMA modulus was 15 kPa. In Fig. 3b, FITC (fluorescein isothiocyanate)-phalloidin staining showed that F-actin, an indispensable component of the cell skeleton, appeared most in BMSCs in the 10% GMPT scaffold compared to the others, suggesting the better cell adhesion properties of 10% GMPT. To further explore cell adhesion on GMPT, SEM was used to record the morphology of BMSCs on the surface of GMPT. We found that BMSCs in the 10% GMPT group had more outstretched lamellipodia extensions than those in the PT, 5% GMPT and 15% GMPT groups (Fig. 3c), which may help explain the adhesion results.

In Fig. 2d, the proliferation ability of BMSCs on scaffolds was evaluated by the CCK-8 assay on days 1, 3, 5, and 7. During the first 5 days, the number of BMSCs was much more significantly increased in the 10% GMPT group, while on day 7, all groups displayed no significant difference from each other (Fig. 3d). The above results indicated that all

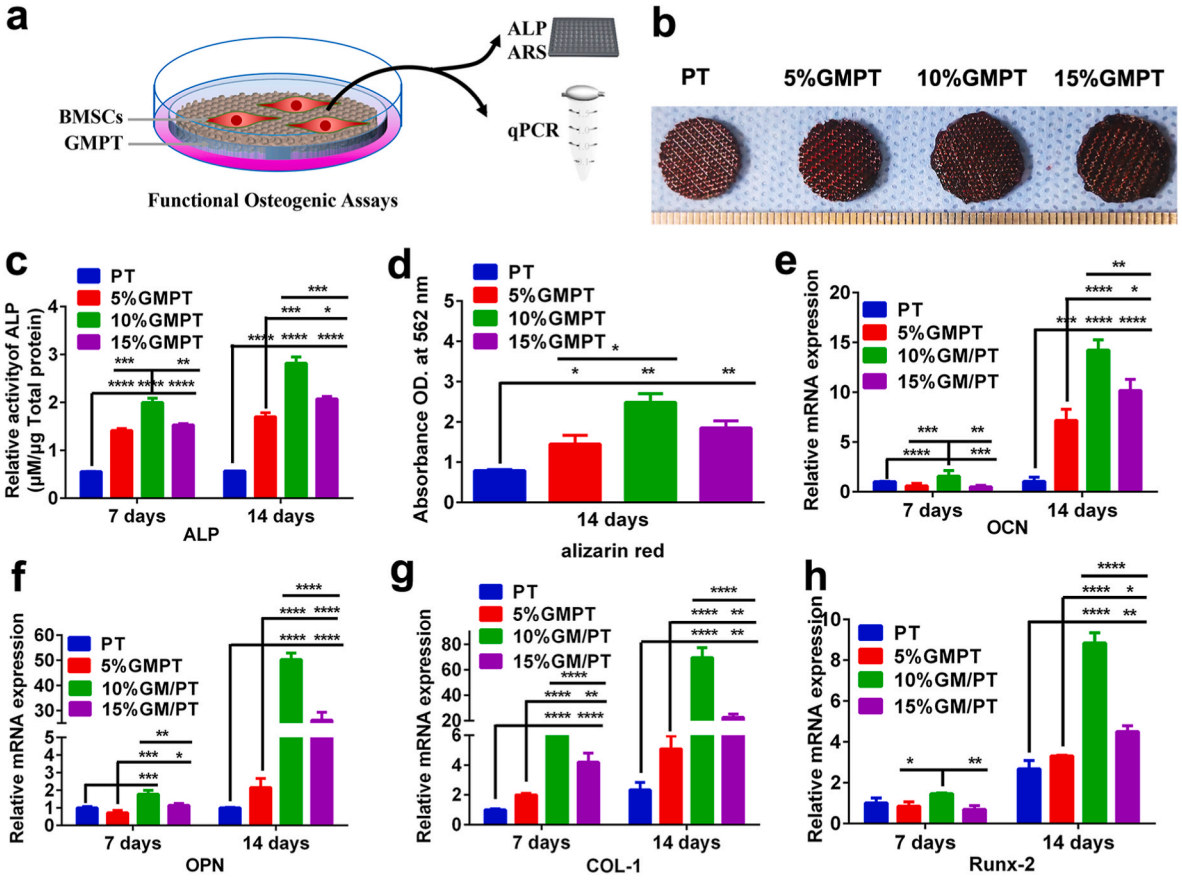

Fig. 4. ***In vitro*** **analysis of osteogenesis on PT and GMPT scaffolds.** (a) Schematic of the experiment. Cells were collected from each group after 7 days and 14 days of incubation. HUVECs were sorted into different groups and used in subsequent experiments. (b) Alizarin red staining images. (c) Quantification of Alizarin red staining through the absorbance value of osteogenesis of PT, 5% GMPT, 10% GMPT and 15% GMPT for 14 days. (d) ALP activity of PT, 5% GMPT, 10% GMPT and 15% GMPT on days 7 and 14. (e–h) The RT-PCR results of osteogenesis-associated gene expression of PT, 5% GMPT, 10% GMPT and 15% GMPT for 7 days and 14 days. The results demonstrated that the softer stiffness of GelMA provided a desirable surrounding environment for osteogenesis, among which 10% GMPT induced a higher level of osteogenic gene expression. Asterisks indicate significant differences, * represents $P < 0.05$, ** represents $P < 0.01$, *** represents $P < 0.001$ and **** represents $P < 0.0001$.

scaffolds showed excellent cytocompatibility, among which 10% GMPT serves as the most desirable environment for cell attachment and proliferation, laying the foundation for tissue regeneration. The blood compatibility of the PT and GMPT scaffolds was investigated by hemolysis assay, and the results showed that the hemolysis rates of all scaffolds were less than 5% (Fig. S6), indicating that the scaffolds are safe for potential clinical application.

3.3. Osteogenesis of PT and GMPT scaffolds

Cells were collected from each group to perform different experiments to identify the best osteogenesis conditions (Fig. 4a). Alizarin red staining experiments were used to verify the mineralization (a marker of osteogenic differentiation in the late stage) of BMSCs on the scaffold surface. On day 14, the 5%, 10%, and 15% (w/v) GMPT groups all had higher staining than the PT control group (Fig. 4b). The quantification of the staining using the relative absorbance value confirmed this observation. More matrix mineralization was seen in the 10% GMPT group than in the other GMPT groups (Fig. 4c). Additionally, the activity of ALP (alkaline phosphatase), an essential early osteogenic marker for the osteogenesis of BMSCs, was examined. On day 7, the 5%, 10% and 15% GMPT groups all had significantly higher ALP activity than the PT group, while the 10% GMPT group possessed the highest ALP activity. The same phenomenon was also observed on day 14 (Fig. 4d). These results indicated that the introduction of GelMA could provide soft media to promote ALP expression and ECM mineralization for osteogenesis, which is consistent with previous studies [28]. Specifically, 10% GMPT presented optimal osteogenic differentiation outcomes, both in the early and late stages.

To further confirm our observation, the levels of osteogenic-related genes (OCN, OPN, Col-I and Runx2) were tested using RT-PCR. On day 7, osteogenic gene expression was low in each group, except for 10% GMPT. On day 14, there was significantly increased osteogenic gene expression in all three GMPT groups compared with the PT group, indicating the ability of GelMA to enhance osteogenic differentiation. Inconsistent with the ALP activity and Alizarin red staining results, BMSCs in the 10% GMPT group showed the best osteogenic differentiation, with markedly increased gene expression compared with the other GMPT groups (Fig. 4e–h).

3.4. Angiogenesis of the PT and GMPT scaffolds

Angiogenesis is vital to provide enough nutrition and bioactive agents for bone regeneration [29], and previous reports showed that GelMA could promote the angiogenic process [30]. The tube formation test was used to evaluate angiogenesis with GMPT (Fig. 5a). The tube formation assays showed that HUVECs cultured with medium containing 10% GMPT formed a capillary-like network with typically closed structures. Incubation of HUVECs in the 10% GMPT group resulted in a longer network of tube-like structures than that in the other groups (Fig. 5b). The migrated HUVECs promoted by BMSCs cultured on GMPT scaffolds were evaluated by Transwell migration assays and wound healing tests. We found that in the 10% GMPT group, more cells migrated (Figs. S7a–b), and the healing rate was faster (Figs. S7c–d).

The representative fluorescent images showed that more vessel segments were formed in the 10% GMPT and 15% GMPT groups than in the 5% GMPT and PT groups (Fig. 5c). Moreover, the detection of angiogenesis-related genes enables the outcomes to be verified at the gene level. In detail, the expression of VEGF, an early angiogenesis marker [31], was observed to be significantly higher in the GMPT groups than in the PT group on day 3 and day 10, and the highest expression was found in the 10% GMPT groups (Fig. 5d). In addition, the expression of HIF-α, KDR and SMAD-1 reflects the angiogenic process [32]. The RT-PCR results of these related genes showed the highest expression in the 10% GMPT group (Fig. 5e–g), and the levels of the above genes expressed in each GMPT group were considerably higher than those in

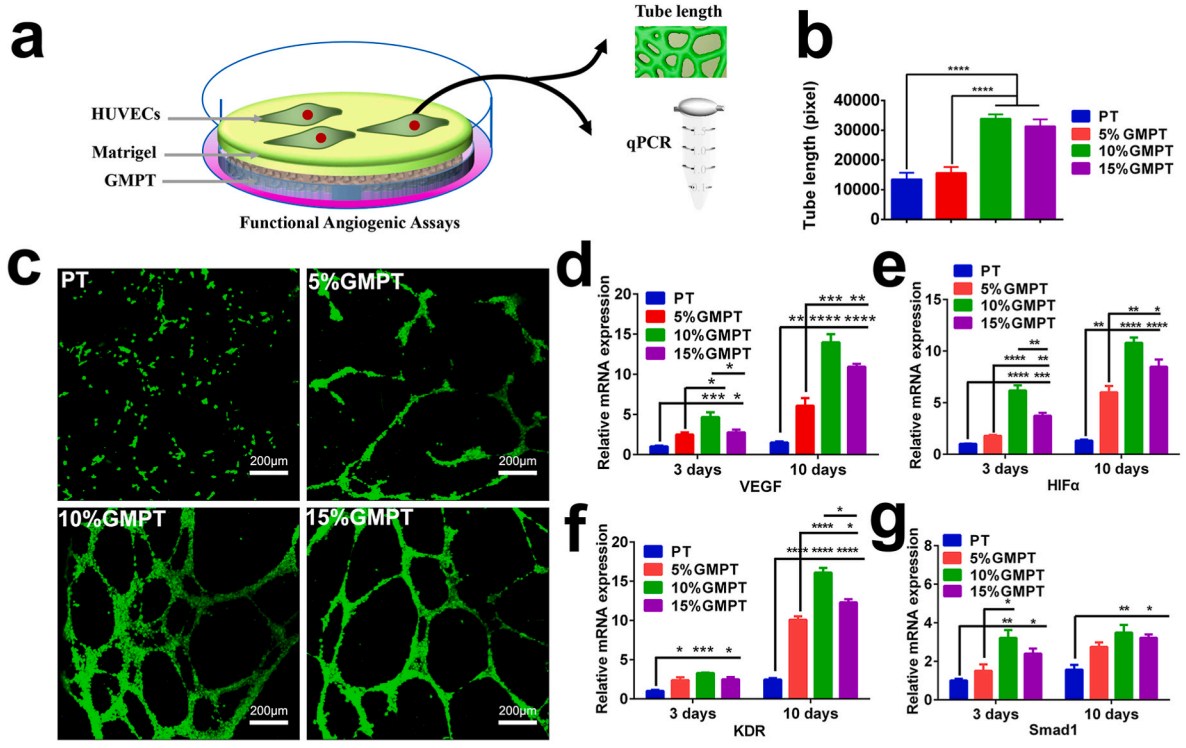

Fig. 5. ***In vitro*** **angiogenesis of PT and GMPT scaffolds.** (a) Schematic of the tubule formation of HUVECs cultured on PT, 5% GMPT, 10% GMPT and 15% GMPT for 24 h. (b) Tubular length of different groups. (c) Immunofluorescence of tube formation. Scale bar, 200 μm. (d–g) The RT-PCR results of angiogenesis-associated gene expression of PT, 5% GMPT, 10% GMPT and 15% GMPT for 3 days and 10 days. The *in vitro* results proved that 10% GMPT provided a better environment for angiogenesis. Asterisks indicate significant differences, *represents $P < 0.05$, ** represents $P < 0.01$, *** represents $P < 0.001$, **represents $P < 0.0001$.

the PT group, which is consistent with the VEGF tendency. Therefore, 10% GelMA is the optimal concentration for GMPT scaffolds, exhibiting the highest activity for both osteogenesis and angiogenesis.

3.5. Gene expression and bioinformatic analysis of the 10% GMPT scaffold

The stiffness of GelMA could modulate the extent of vascular network formation [33]. For example, Huebsch and his colleagues demonstrated that the osteogenic differentiation of the MSCs occurred predominantly at 11–30 kPa, especially at 22 kPa in the 3D hydrogel [33,34]. In addition, GelMA can regulate metalloproteinase activity, and its osteon-like structure will favor osteogenesis and angiogenesis [35,36]. Our above-obtained results were consistent with these researches, but the underlying mechanism is not clear. Therefore, we performed RNA-Seq on the GMPT scaffold at 24 h using the Illumina NovaSeq 6000 sequence platform. For convenience of analysis, we sequenced the 10% GMPT group, which has the most significant osteogenesis and angiogenesis effects. In addition, PT was set as a control. As shown in the volcano plots of all detected and expressed genes (Fig. 6a), the differentially expressed gene clusters revealed that 821 genes were upregulated and 2421 genes were downregulated. Based on gene ontology (GO) annotations of significantly different genes, we found that numerous angiogenesis-related genes, such as Cxcl12, Ccn3, Srpx2, Thy1, and Emc10 (Fig. 6b), and ossification reaction-related genes, including Nid2, Ccn1, Ptn, Clec3b, Lrrc17, etc., were upregulated in 10% GMPT (Fig. 6c). These results were consistent with the *in vitro* angiogenic and osteogenic experiments.

We next conducted Kyoto Encyclopedia of Genes and Genomes (KEGG) pathway analysis to further study the underlying mechanism. The top enriched pathways of upregulated genes for the two groups are shown in Fig. 6d. The results revealed that differentially expressed genes were enriched in the cell cycle, focal adhesion pathway and PI3K-AKT pathways, which were the suggested pathways for the regulation of angiogenesis and osteogenesis during the bone repair process. Previous research showed that cell proliferation increased during osteogenesis [37], indicating the induction of the “cell cycle” pathway. Tuning the material surface stiffness allows the modulation of cell adhesion, proliferation, and differentiation, showing that the focal adhesion pathway has an important impact on angiogenesis and osteogenesis [38]. The PI3K/AKT/mTOR pathway is an intracellular signaling pathway that controls the cell cycle. Phosphorylation of PI3K activates downstream AKT, which regulates phosphorylation of mTOR. Researchers have found that activation of the PI3K/AKT/mTOR pathway is a common feature of angiogenesis [39] and osteogenesis [40]. Importantly, PI3K/AKT is an activated signaling pathway when ECM stiffness increases within a certain range; this process requires the scaffold to possess tunable mechanical properties to optimize cell differentiation. A suitable “soft” environment can activate the angiogenic and osteogenic signals of adhered cells through the focal adhesion pathway and the downstream PI3K/AKT pathway.

To further confirm the activation of the PI3K-AKT pathway, intracellular flow cytometry (FCM) was conducted to test the phosphorylation of PI3K, AKT and mTOR in the PT, 5% GMPT, 10% GMPT and 15% GMPT groups (Fig. 6e–g). The results demonstrated that the phosphorylation rate of the 10% GMPT group was the highest. Overall, based on the results of RNA-seq and FCM, we can conclude that the 10% GMPT scaffold can effectively promote bone and vascular regeneration, and the PI3K/AKT/mTOR pathway is an important candidate pathway.

3.6. In situ radius bone defect repair using GMPT scaffolds

The 10% GMPT group showed more desirable osteogenesis and angiogenesis effects than the 5% GMPT and 15% GMPT groups *in vitro*. However, the question remained of whether 10% GMPT could also demonstrate the best bone regeneration *in vivo*. Therefore, the rabbit radius defect model was used to study the *in vivo* stimulatory effect of GMPT scaffolds for bone regeneration, as shown in Fig. 7a–b. After 4 weeks of surgery, the 3D reconstruction micro-CT images showed that significantly newly formed bone was observed in all GMPT groups, which was more than that in the PT group. The volumes of the regenerated bone were in the following order: 10% GMPT>15% GMPT>5% GMPT > PT (Fig. 7c). Furthermore, quantitative analysis of new bone formation, which was denoted as the volume ratio of new bone and total tissue (BV/TV), was conducted using the PT group as a control. The results illustrated that at week 4, the BV/TV results of 5% GMPT, 10% GMPT, and 15% GMPT were 1.12, 1.41, and 1.16 times that of the control group, respectively. After 12 weeks, the difference tendency was further expanded, of which the regenerated bone volumes in the 5% GMPT, 10% GMPT, and 15% GMPT groups were 1.48, 2.05, and 1.54 times that of the control group (Fig. 7d), indicating the optimal osteogenic ability of the 10% GMPT scaffolds.

In addition, two more tests were carried out to test the immobility of osseointegration. One test assessed the bone mineral density (BMD), and the other involved direct mechanical testing, which reflects the biomechanical properties of the repaired bone tissues. A greater BMD level was present in the GMPT groups than in the PT scaffolds at weeks 4 and 12. Unsurprisingly, the newly formed bone in the 10% GMPT group still showed the highest bone density (Fig. 7e). The mechanical test results showed that the maximum load in the GMPT group was statistically higher than that in the control group, among which the maximum load in the 10% GMPT group was the maximum (Fig. 7f–g), suggesting the best osseointegration of the 10% GMPT scaffold.

As shown in Fig. 8, the Van Gieson picro-fuchsin staining results can help histologically analyze the osteointegration and angiogenesis effects of the GMPT scaffolds. On week 4, although little regenerated bone was observed in each group, more trabeculae were found around the GMPT scaffolds than in the PT group, especially in the 10% GMPT group. On week 12, more new bone was formed around the scaffolds, with the trabeculae becoming more regular and thicker. However, markedly more new bone was formed in the GMPT groups than in the PT group, with the most development in the 10% GMPT group. In addition, gaps were found between the new bone and the scaffolds, except for the 10% GMPT group, indicating that this group had the best osteointegration. According to the histology analysis, more vessels were formed within the GMPT scaffolds, especially in the 10% GMPT group, which is consistent with the *in vitro* tubule formation results.

Masson’s trichrome staining results also exhibited a similar tendency (Fig. S8). Woven bone emerged in all groups at week 4, followed by further transformation into mature lamellar bone with Haversian osteons at week 12. Similarly, much more integrity and maturity of the healed bone was found in the GMPT groups than in the PT group, and the 10% GMPT group still possessed the most desirable outcomes. Interestingly, we found that new bone first formed around the scaffolds and then filled the macropores of the scaffolds. This kind of bone regeneration behavior is beneficial to nutrition communication within the scaffold in the early stage of bone repair, leading to an increased bone ingrowth depth [41].

Angiogenesis of the scaffold could provide sufficient nutrition to support bone reconstruction. CD31, also known as platelet-endothelial cell adhesion molecule-1 (PECAM-1), plays a role in cell adhesion and is considered a biomarker of endothelial cells [42]. Additional immunofluorescence CD31 staining was conducted to analyze the angiogenesis of the scaffolds (Fig. 9). The yellow arrows in the stained images indicate the newly formed vessels. Compared with the PT groups, the GMPT groups presented significantly more formed blood vessels. The 10% GMPT group showed the most concentrated expression, indicating the most mature formation of vessels.

Overall, the *in vivo* results were consistent with the *in vitro* results, proving that a suitable GMPT design could significantly enhance osteogenesis and angiogenesis, and the GMPT scaffold with 10% GelMA presented the optimum effect.

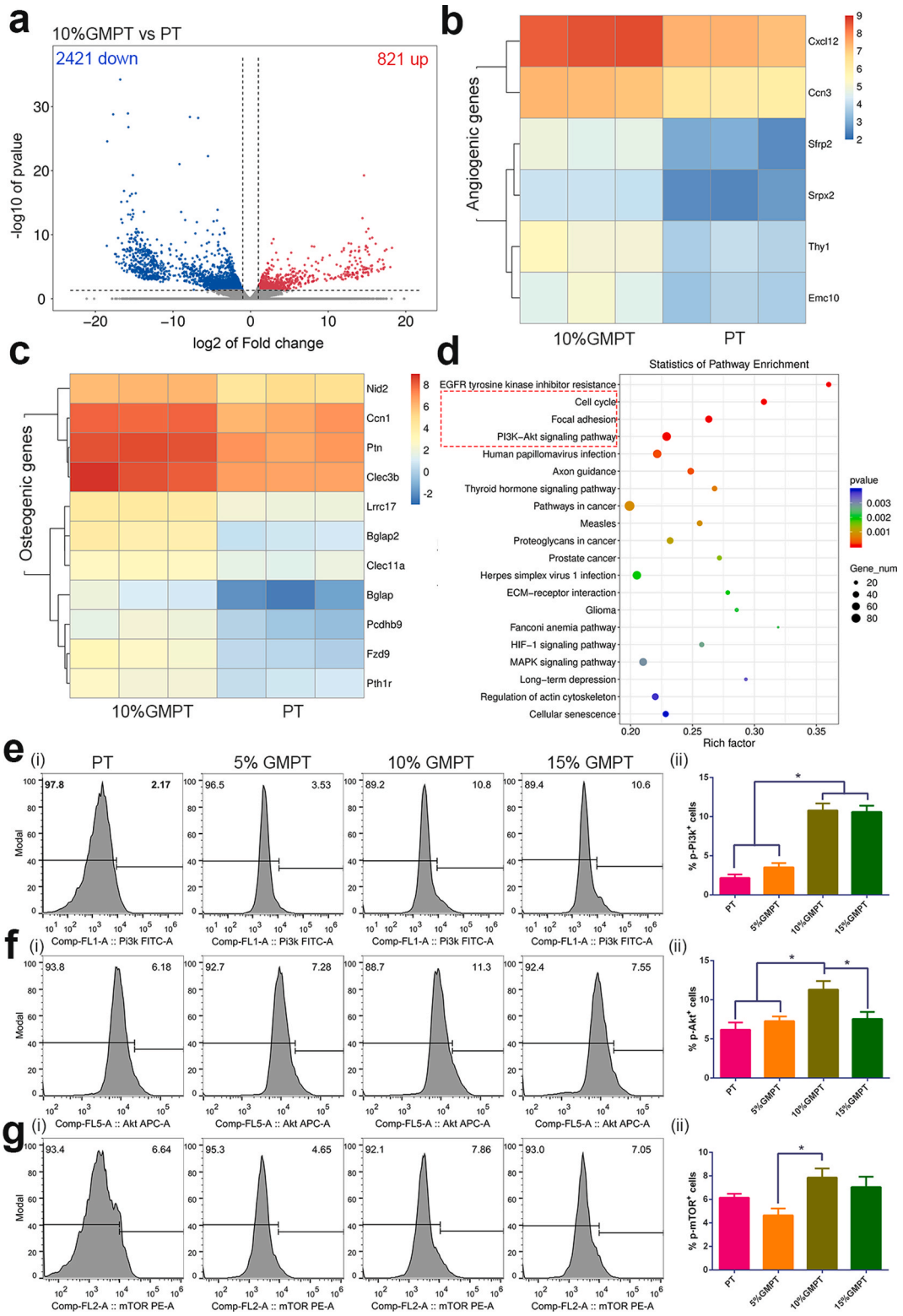

Fig. 6. Gene expression and bioinformatic analysis across the 10% GMPT scaffold. (a) Volcano plot of the differentially expressed genes between groups. (≥2-fold difference; red: upregulated genes; blue: downregulated genes). (b) Heat map of angiogenesis-related gene expression. (c) Heat map of osteogenesis-related gene expression. (red: high expression; blue: low expression). (d) The gene enrichment KEGG pathway analysis. (e–g) Intracellular flow cytometry (FCM) for the phosphorylation of Pi3k (e), Akt (f) and mTOR (g) in the PT, 5% GMPT, 10% GMPT and 15% GMPT groups, where (i) are FCM figures and (ii) are their quantitation results. Asterisks indicate significant differences, *represents $P < 0.05$.

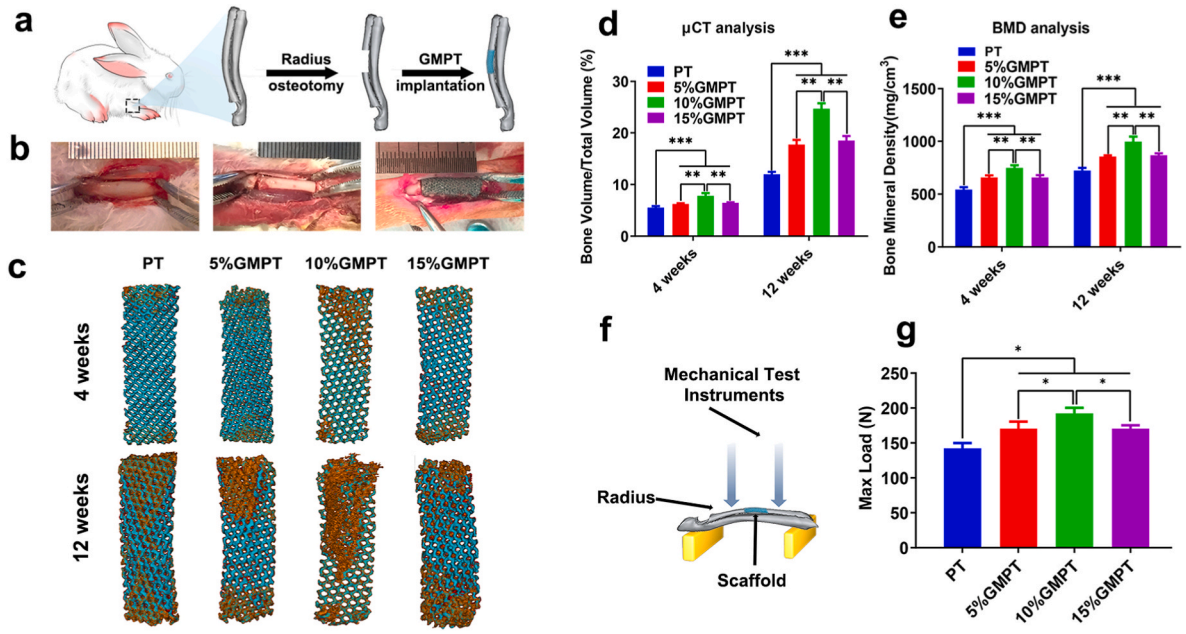

Fig. 7. In situ implantation of PT and GMPT scaffolds, micro-CT 3D reconstruction and biomechanical test of PT and GMPT in critical radius defects of rabbits. (a) Schematic illustration of GMPT *in vivo* implantation. (b) The surgical process of GMPT implantation in rabbits with critical radius defects. (c) Micro-CT reconstruction of bone regeneration with the scaffolds at 4 and 12 weeks postsurgery. The new bones were brown color. (d) Bone volume/total volume (BV/TV) analysis of the bone defect 4 and 12 weeks after surgery. (e) Bone mineral density (BMD) analysis of regenerated bone 4 and 12 weeks after surgery. (f) Schematic illustration of the direct mechanical testing for *in vivo* samples. (g) The maximum load of direct mechanical testing for implanted scaffolds. These results demonstrated that the prognosis of in situ implantation of GMPT scaffolds in critical radius defects was preferable to that of PT scaffolds. Overall, 10% GMPT showed the best results, in accordance with the *in vitro* test. *represents $P < 0.05$, ** represents $P < 0.01$, *** represents $P < 0.001$.

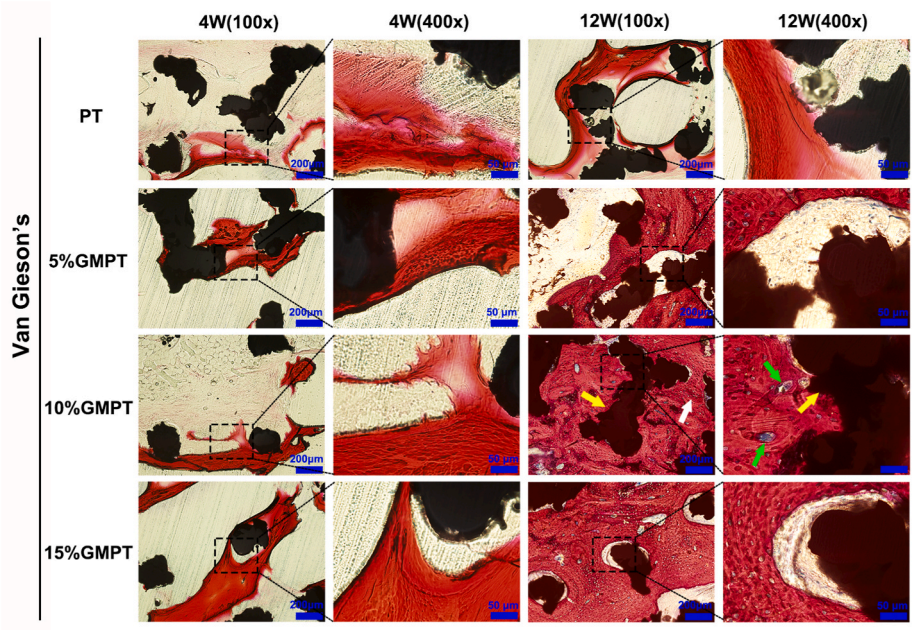

Fig. 8. Histological analysis of implant samples after 4 and 12 weeks in rabbit radius defect sites. Van Gieson's staining of the PT and GMPT scaffolds at 4 and 12 weeks after the operation was carried out to evaluate osteogenesis and angiogenesis. The GMPT group showed thicker and more trabeculae than the PT group at both weeks 4 and 12 (yellow arrows indicate the PT scaffold, white arrows indicate new bone, green arrows reveal new vessels). The 10% GMPT group showed the best osteogenesis and angiogenesis ability.

4. Conclusion

In summary, we have developed a TC4/GelMA hybrid scaffold with dual bionic features for the repair of large bone defects. In our system, a "hard" 3D-printed PT backbone was chemically functionalized with a "soft" GelMA hydrogel to mimic the heterogeneous microstructure and mechanical properties of natural bone tissue. Compared with pure PT implants, the soft hydrogel in the scaffold provided a favoring platform for the attachment and differentiation of BMSCs. By optimizing the GelMA concentration, GMPT at a concentration of 10% (14.46 ± 1.55 kPa) showed the best capability of promoting cell attachment and differentiation. The RNA-seq and FCM results revealed the underlying mechanism by which the angiogenesis and osteogenesis processes of 10% GMPT were regulated by PI3K/AKT/mTOR signaling. This work shows that a bioactive soft surface with suitable stiffness is vital for hard metal implants to achieve better osteointegration, which is likely to broaden the horizons for the design of next-generation large bone defect implants.

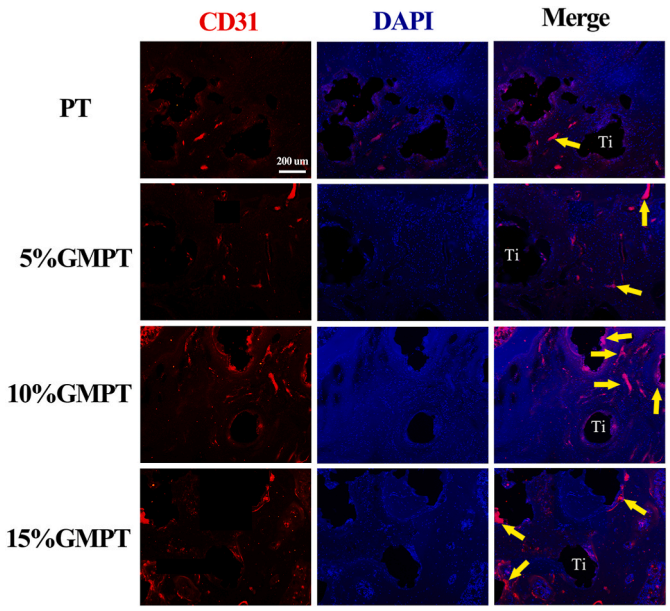

Fig. 9. CD31 immunofluorescence staining images of the vessel around scaffolds. Yellow arrows indicate the formed blood vessels. The staining area was distributed sporadically in the PT group, while in the GMPT groups, highly concentrated staining was observed. The 10% GMPT group had more mature vessels formed than the other GMPT groups.

Declaration of competing interestCOI

The authors declare no competing financial interest.

CRediT authorship contribution statement

Limin Ma: Methodology, Investigation, Data curation, Formal analysis, Funding acquisition, Writing – original draft. **Xiaolan Wang:** Methodology, Investigation, Data curation, Formal analysis, Writing – original draft. **Ye Zhou:** Methodology, Investigation, Data curation, Formal analysis, Writing – original draft. **Xiongfa Ji:** Investigation, Validation, Methodology. **Shi Cheng:** Investigation, Formal analysis. **Dong Bian:** Data curation. **Lei Fan:** Methodology, Formal analysis. **Lei Zhou:** Methodology, Project administration, Supervision, Writing – review & editing. **Chengyun Ning:** Methodology, Project administration, Supervision, Writing – review & editing. **Yu Zhang:** Methodology, Project administration, Supervision, Funding acquisition, Writing – review & editing.

Acknowledgments

This work was supported by National Natural Science Foundation of China (31700880, 81972126), Natural Science Foundation of Guangdong Province (2020A1515010827), Science and Technology Planning Project of Guangzhou city (201803010106), The China Postdoctoral Science Foundation (2019M652957), Science and Technology Planning Project of Jiangmen City (2019030102490013068), and the High-level Hospital Construction Project (KJ012019100) for financial support.

Appendix A. Supplementary data

Supplementary data to this article can be found online at https://doi.org/10.1016/j.bioactmat.2021.03.010.

References

[1] R. Agarwal, A.J. Garcia, Biomaterial strategies for engineering implants for enhanced osseointegration and bone repair, Adv. Drug Deliv. Rev. 94 (2015) 53–62.
[2] H. Petite, V. Viateau, W. Bensaïd, A. Meunier, C.D. Pollak, M. Bourguignon, et al., Tissue-engineered bone regeneration, Nat. Biotechnol. 18 (2000) 959.
[3] J. Biggemann, M. Pezoldt, M. Stumpf, P. Greil, T. Fey, Modular ceramic scaffolds for individual implants, Acta Biomater. 80 (2018) 390–400.
[4] J.C. Reichert, A. Cipitria, D.R. Epari, S. Saifzadeh, P. Krishnakanth, A. Berner, et al., A tissue engineering solution for segmental defect regeneration in load-bearing long bones, Sci. Transl. Med. 4 (2012) 141ra93.
[5] M. Larsen, M. Pelzer, P.F. Friedrich, C.M. Wood, A.T. Bishop, Living bone allotransplants survive by surgical angiogenesis alone: development of a novel method of composite tissue allotransplantation, J. Bone Joint Surg. Am. 93 (2011) 261–273.
[6] H. Ito, M. Koefoed, P. Tiyapatanaputi, K. Gromov, J.J. Goater, J. Carmouche, et al., Remodeling of cortical bone allografts mediated by adherent rAAV-RANKL and VEGF gene therapy, Nat. Med. 11 (2005) 291–297.
[7] M. Bez, D. Sheyn, W. Tawackoli, In situ bone tissue engineering via ultrasound-mediated gene delivery to endogenous progenitor cells in mini-pigs, Sci. Transl. Med. 9 (2017), eaal3128.
[8] S. Bose, M. Roy, A. Bandyopadhyay, Recent advances in bone tissue engineering scaffolds, Trends Biotechnol. 30 (2012) 546–554.
[9] A.M. Pobloth, S. Checa, H. Razi, A. Petersen, J.C. Weaver, K. Schmidt-Bleek, et al., Mechanobiologically optimized 3D titanium-mesh scaffolds enhance bone regeneration in critical segmental defects in sheep, Sci. Transl. Med. 10 (2018) eaam8828.
[10] S. Barui, A.K. Panda, S. Naskar, R. Kuppuraj, S. Basu, B. Basu, 3D inkjet printing of biomaterials with strength reliability and cytocompatibility: quantitative process strategy for Ti-6Al-4V, Biomaterials 213 (2019) 119212.
[11] S. Mei, H. Wang, W. Wang, L. Tong, H. Pan, C. Ruan, et al., Antibacterial effects and biocompatibility of titanium surfaces with graded silver incorporation in titania nanotubes, Biomaterials 35 (2014) 4255–4265.
[12] L.-Y. Chen, Y.-W. Cui, L.-C. Zhang, Recent development in beta titanium alloys for biomedical applications, Metals 10 (2020) 1139.
[13] W. Zhao, D. Michalik, S. Ferguson, W. Hofstetter, J. Lemaitre, Rapid evaluation of bioactive Ti-based surfaces using an in vitro titration method, Nat. Commun. 10 (2019) 2062.
[14] T. Zhou, L. Yan, C. Xie, P. Li, L. Jiang, J. Fang, et al., A mussel-inspired persistent ROS-scavenging, electroactive, and osteoinductive scaffold based on electrochemical-driven in situ nanoassembly, Small 15 (2019), 1805440.
[15] L. Ma, X. Wang, N. Zhao, Y. Zhu, Z. Qiu, Q. Li, et al., Integrating 3D printing and biomimetic mineralization for personalized enhanced osteogenesis, angiogenesis, and osteointegration, Acs Appl. Mater. Inter. 10 (2018) 42146–42154.
[16] L.-C. Zhang, L.-Y. Chen, L. Wang, Surface modification of titanium and titanium alloys: technologies, developments, and future interests, Adv. Eng. Mater. 22 (2020), 1901258.
[17] X.-Y. Ma, Y.-F. Feng, Z.-S. Ma, X. Li, J. Wang, L. Wang, et al., The promotion of osteointegration under diabetic conditions using chitosan/hydroxyapatite composite coating on porous titanium surfaces, Biomaterials 35 (2014) 7259–7270.
[18] X. Wang, S. Xu, S. Zhou, W. Xu, M. Leary, P. Choong, et al., Topological design and additive manufacturing of porous metals for bone scaffolds and orthopaedic implants: a review, Biomaterials 83 (2016) 127–141.
[19] P. Gao, B. Fan, X. Yu, W. Liu, J. Wu, L. Shi, et al., Biofunctional magnesium coated Ti6Al4V scaffold enhances osteogenesis and angiogenesis in vitro and in vivo for orthopedic application, Bioact Mater 5 (2020) 680–693.
[20] C. McBeth, J. Lauer, M. Ottersbach, J. Campbell, A. Sharon, A.F. Sauer-Budge, 3D bioprinting of GelMA scaffolds triggers mineral deposition by primary human osteoblasts, Biofabrication 9 (2017), 015009.
[21] S.-y. He, Y. Zhang, Y. Zhou, N. Bao, Y. Cai, P. Zhou, et al., Modeling osteoinduction in titanium bone scaffold with a representative channel structure, Mat. Sci. Eng. C-Mater. 117 (2020), 111347.
[22] P. Ouyang, H. Dong, X. He, X. Cai, Y. Wang, J. Li, et al., Hydromechanical mechanism behind the effect of pore size of porous titanium scaffolds on osteoblast response and bone ingrowth, Mater. Des. 183 (2019), 108151.
[23] D. Loessner, C. Meinert, E. Kaemmerer, L.C. Martine, K. Yue, P.A. Levett, et al., Functionalization, preparation and use of cell-laden gelatin methacryloyl-based hydrogels as modular tissue culture platforms, Nat. Protoc. 11 (2016) 727–746.
[24] J.W. Nichol, S.T. Koshy, H. Bae, C.M. Hwang, S. Yamanlar, A. Khademhosseini, Cell-laden microengineered gelatin methacrylate hydrogels, Biomaterials 31 (2010) 5536–5544.
[25] N. van Gastel, S. Stegen, G. Eelen, S. Schoors, A. Carlier, V.W. Daniëls, et al., Lipid availability determines fate of skeletal progenitor cells via SOX9, Nature 579 (2020) 111–117.
[26] R. Beekman, V. Chapaprieta, The reference epigenome and regulatory chromatin landscape of chronic lymphocytic leukemia, Nat. Med. 24 (2018) 868–880.
[27] C. Feng, W. Zhang, C. Deng, G. Li, J. Chang, Z. Zhang, et al., 3D printing of Lotus root-like biomimetic materials for cell delivery and tissue regeneration, Adv. Sci. 4 (2017) 1700401.
[28] X. Fang, J. Xie, L. Zhong, J. Li, D. Rong, X. Li, et al., Biomimetic gelatin methacrylamide hydrogel scaffolds for bone tissue engineering, J. Mater. Chem. B 4 (2016) 1070–1080.
[29] K. Hu, B.R. Olsen, Osteoblast-derived VEGF regulates osteoblast differentiation and bone formation during bone repair, J. Clin. Invest. 126 (2016) 509–526.

[30] Y.C. Chen, R.Z. Lin, H. Qi, Y. Yang, H. Bae, J.M. Melero-Martin, et al., Functional human vascular network generated in photocrosslinkable gelatin methacrylate hydrogels, Adv. Funct. Mater. 22 (2012) 2027–2039.
[31] K.L. Spiller, R.R. Anfang, K.J. Spiller, J. Ng, K.R. Nakazawa, J.W. Daulton, et al., The role of macrophage phenotype in vascularization of tissue engineering scaffolds, Biomaterials 35 (2014) 4477–4488.
[32] Q. Yao, Y. Liu, B. Selvaratnam, R.T. Koodali, H. Sun, Mesoporous silicate nanoparticles/3D nanofibrous scaffold-mediated dual-drug delivery for bone tissue engineering, J. Contr. Release 279 (2018) 69–78.
[33] Y.C. Chen, R.Z. Lin, H. Qi, Y. Yang, H. Bae, J.M. Melero-Martin, et al., Functional human vascular network generated in photocrosslinkable gelatin methacrylate hydrogels, Adv. Funct. Mater. 22 (2012) 2027–2039.
[34] N. Huebsch, P.R. Arany, A.S. Mao, D. Shvartsman, O.A. Ali, S.A. Bencherif, et al., Harnessing traction-mediated manipulation of the cell/matrix interface to control stem-cell fate, Nat. Mater. 9 (2010) 518–526.
[35] K. Yue, G. Trujillo-de Santiago, M.M. Alvarez, A. Tamayol, N. Annabi, A. Khademhosseini, Synthesis, properties, and biomedical applications of gelatin methacryloyl (GelMA) hydrogels, Biomaterials 73 (2015) 254–271.
[36] Y. Zuo, W. Xiao, X. Chen, Y. Tang, H. Luo, H. Fan, Bottom-up approach to build osteon-like structure by cell-laden photocrosslinkable hydrogel, Chem Commun (Camb) 48 (2012) 3170–3172.
[37] K.-S. Tsai, S.-Y. Kao, C.-Y. Wang, Y.-J. Wang, J.-P. Wang, S.-C. Hung, Type I collagen promotes proliferation and osteogenesis of human mesenchymal stem cells via activation of ERK and Akt pathways, J. Biomed. Mater. Res. A 94A (2010) 673–682.
[38] A. Wilkinson, R.N. Hewitt, L.E. McNamara, D. McCloy, R.M. Dominic Meek, M. J. Dalby, Biomimetic microtopography to enhance osteogenesis in vitro, Acta Biomater. 7 (2011) 2919–2925.
[39] J. Karar, A. Maity, PI3K/AKT/mTOR pathway in angiogenesis, Front. Mol. Neurosci. 4 (2011) 51.
[40] N. Baker, J. Sohn, R.S. Tuan, Promotion of human mesenchymal stem cell osteogenesis by PI3-kinase/Akt signaling, and the influence of caveolin-1/cholesterol homeostasis, Stem Cell Res. Ther. 6 (2015) 238.
[41] K. Zhou, P. Yu, X. Shi, T. Ling, W. Zeng, A. Chen, et al., Hierarchically porous hydroxyapatite hybrid scaffold incorporated with reduced graphene oxide for rapid bone ingrowth and repair, ACS Nano 13 (2019) 9595–9606.
[42] H. Sauer, M.M. Bekhite, J. Hescheler, M. Wartenberg, Redox control of angiogenic factors and CD31-positive vessel-like structures in mouse embryonic stem cells after direct current electrical field stimulation, Exp. Cell Res. 304 (2005) 380–390.